

On-chip positionable photonic waveguides for chip-to-chip optical interconnects

Peters, Tjitte Jelte; Tichem, Marcel

DOI

[10.1117/12.2222512](https://doi.org/10.1117/12.2222512)

Publication date

2016

Document Version

Final published version

Published in

Silicon Photonics and Photonic Integrated Circuits V

Citation (APA)

Peters, T. J., & Tichem, M. (2016). On-chip positionable photonic waveguides for chip-to-chip optical interconnects. In L. Vivien, L. Pavesi, & S. Pelli (Eds.), *Silicon Photonics and Photonic Integrated Circuits V* (Vol. 9891). Article 98911S (Proceedings of SPIE; Vol. 9891). SPIE. <https://doi.org/10.1117/12.2222512>

Important note

To cite this publication, please use the final published version (if applicable). Please check the document version above.

Copyright

Other than for strictly personal use, it is not permitted to download, forward or distribute the text or part of it, without the consent of the author(s) and/or copyright holder(s), unless the work is under an open content license such as Creative Commons.

Takedown policy

Please contact us and provide details if you believe this document breaches copyrights. We will remove access to the work immediately and investigate your claim.

PROCEEDINGS OF SPIE

[SPIDigitalLibrary.org/conference-proceedings-of-spie](https://spiedigitallibrary.org/conference-proceedings-of-spie)

On-chip positionable photonic waveguides for chip-to-chip optical interconnects

Tjitte-Jelte Peters
Marcel Tichem

SPIE.

On-chip positionable photonic waveguides for chip-to-chip optical interconnects

Tjitte-Jelte Peters and Marcel Tichem

Delft University of Technology, Department of Precision and Microsystems Engineering,
Mekelweg 2, 2628 CD Delft, Netherlands

ABSTRACT

This paper reports on the progress related to a multichannel photonic alignment concept, aiming for submicrometer precision in the alignment of the waveguides of two photonic integrated circuits (PICs). The concept consists of two steps: chip-to-chip positioning and chip bonding provide a coarse alignment after which waveguide-to-waveguide positioning and fixing result in a fine alignment. For the waveguide-to-waveguide alignment, an alignment functionality is developed and integrated in one of the PICs, consisting of mechanically flexible waveguides and MEMS actuators. This paper reports on the fabrication and characterization of a mechanically flexible waveguide array that can be positioned by two out-of-plane actuators.

Thermal actuators are integrated with mechanically flexible waveguide beams to enable positioning them with high precision. By adding a poly-Si pattern on top of SiO₂ beams, an out-of-plane bimorph actuator can be realized. An analytical model enables estimating the curvature and the deflection of a single bimorph beam. Acquiring a small initial deflection while having a large motion range of the actuator proves to have conflicting demands on the poly-Si / SiO₂ thickness ratio.

In this paper, we show that suspended waveguide arrays with integrated alignment functionality have an initial deflection – they curl up – due to residual stress in the materials. The actuators can be operated using a driving voltage between 0 V to 45 V, corresponding to ~50 mW. Using higher voltages brings the risk of permanently changing the material properties of the heaters. The actuators can accomplish an out-of-plane crossbar translation up to 6.5 μm at ~50 mW as well as a rotation around the propagation direction of the light ranging from -0.1° to 0.1°. At a constant actuation power of ~50 mW, the crossbar shows a drift in vertical deflection of 0.16 μm over a time of 30 min.

Keywords: Photonics, MEMS, optical interconnect, waveguides, alignment, bimorph actuator, deflection, stability

1. INTRODUCTION

Photonic integrated circuits (PICs) become more affordable as photonic fabrication technologies mature. For example, the cost of material and fabrication of PICs with limited complexity can be as low as €10 per device. However, the developments in assembly and packaging technology are falling behind. No standardized assembly technology is available, but instead, tailored solutions need to be developed for specific assembly configurations. As a result, the packaging process is an order of magnitude more expensive than the fabrication of PICs.

In previous work, an innovative multichannel photonic alignment concept was proposed, motivated by the lack of standardized assembly technology. The concept aims to achieve automated and cost-effective submicrometer alignment of the waveguides of two photonic integrated circuits (PICs). One of these PICs contains active photonic elements, while the other PIC contains passive photonic waveguides and an integrated alignment function. This paper focuses on the development of the integrated alignment functionality.

The alignment concept utilizes chip-to-chip pre-alignment and mounting on a common carrier, followed by waveguide-to-waveguide fine-alignment and waveguide position locking. After the pre-alignment step, some

Further author information: (Send correspondence to M. Tichem)
M. Tichem: E-mail: m.tichem@tudelft.nl
T. Peters: E-mail: t.j.peters@tudelft.nl

misalignment (up to several micrometers) is tolerable in specific degrees of freedom. Low-cost and time-efficient methods, e.g. flip-chip bonding, are suitable to achieve the alignment accuracy required for this pre-alignment step. The final submicrometer alignment is achieved in the fine-alignment stage, using the integrated alignment functionality in one of the PICs.

We propose the integration of microelectromechanical system (MEMS) actuators with mechanically flexible waveguides to enable accurate positioning of the waveguide end-facets. Flexible waveguide arrays are created in PICs that are based on TriPleX technology,¹ i.e. a silicon nitride (Si_3N_4) core encapsulated in a silicon dioxide (SiO_2) cladding. A single flexible waveguide array consists of parallel cantilevered beams and a crossbar that connects the free ends of the beams. Thermal bimorph actuators are realized by adding patterned poly-Si on top of predefined SiO_2 beams. A typical positionable waveguide array consists of a number of waveguide beams in the center with a number of bimorph beams on both sides. The bimorph beams on one side are electrically connected in series, and can be regarded as a set of actuator beams, or simply ‘one actuator’. With this configuration, differential operation of the actuators results in a rotation as well as a small out-of-plane deflection of the crossbar. Simultaneous operation of the actuators produces an out-of-plane translation of the crossbar.

This paper demonstrates the integration of MEMS actuators with mechanically flexible waveguides and characterizes the actuators’ positioning performance. Section 2 investigates the influence of the poly-Si thickness on the integrated alignment functionality. The fabrication process of the suspended structures and the integrated MEMS actuators is presented in section 3. The characterization is described in section 4, covering the initial deflection without actuation as well as the deflection upon actuation. Moreover, the operating range of the actuators and the stability over time are examined. Ultimately, some conclusions and an outlook are provided in section 5.

2. ANALYTICAL BIMORPH BEAM MODEL

The deflection of a single actuator beam can be estimated using a simplified bimorph beam, consisting of two layers with a different coefficient of thermal expansion (CTE). Figure 1 shows a schematic representation of a single bimorph beam, consisting of a SiO_2 beam with a strip of poly-Si on top.

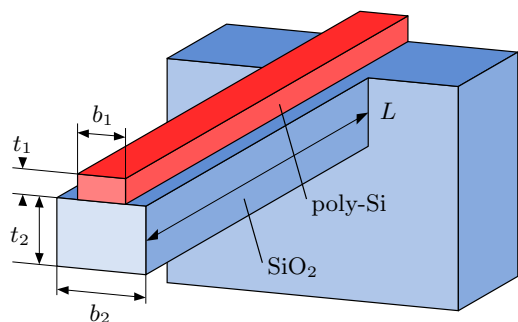


Figure 1: Schematic representation of a simplified bimorph beam, showing the dimensional parameters of both layers.

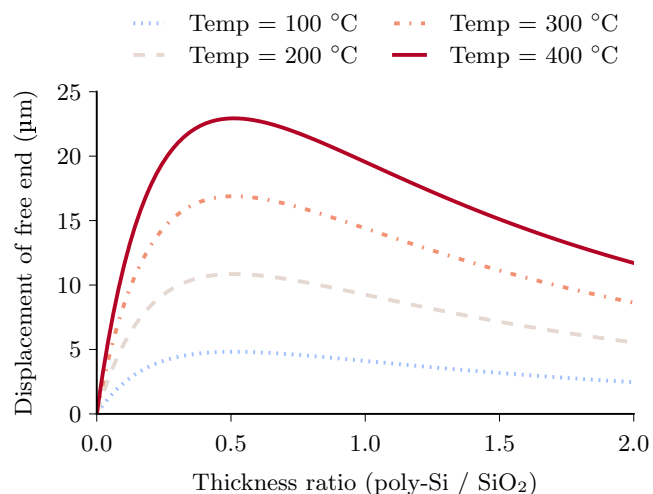


Figure 2: The out-of-plane displacement of a poly-Si / SiO_2 bimorph beam at different temperatures as a function of its layer thickness ratio. A 0 μm displacement corresponds to the situation at room temperature. The displayed curves follow from the analytical model with $b_1=8 \mu\text{m}$, $b_2=18 \mu\text{m}$, $t_2=16 \mu\text{m}$, and $L=800 \mu\text{m}$.

A poly-Si / SiO₂ bimorph beam at room temperature curves upward. This is because at temperatures deviating from the deposition temperature, the different thermal expansion coefficients of poly-Si and SiO₂ introduce thermal stress, causing the beam to bend. The curvature κ of a bimorph beam as a result of a temperature difference ΔT can be written as an analytical function² of the dimensional and mechanical parameters:

$$\kappa = \frac{6\xi_1\xi_2(t_1 + t_2)(\alpha_1 - \alpha_2)\Delta T}{(\xi_1t_1)^2 + (\xi_2t_2)^2 + 2\xi_1\xi_2(3t_1t_2 + 2t_1^2 + 2t_2^2)}, \quad (1)$$

where

$$\begin{aligned} \xi_1 &= b_1t_1E_1, \\ \xi_2 &= b_2t_2E_2, \end{aligned}$$

and b_i , t_i , E_i , and α_i are the width, the thickness, the modulus of elasticity, and the CTE of material i , respectively. Using this equation, the influence of the thickness ratio on the curvature can be analysed.

Moreover, by converting the beam curvature into the displacement of the free end, the motion range of a bimorph beam can be plotted as a function of its thickness ratio. Figure 2 shows the calculated displacement of the free end as a function of poly-Si / SiO₂ thickness ratio at different temperatures. A 0 μm displacement corresponds to the situation at room temperature. This graph is based on a bimorph beam with a length of 800 μm , a SiO₂ thickness of 16 μm , a SiO₂ width of 18 μm , and a poly-Si width of 8 μm . The displacement curves reveal that the maximum displacement is realized with a poly-Si thickness that is approximately half the SiO₂ thickness. However, this maximum motion range coincides with a maximum bimorph curvature at room temperature, because the displacement is a result of the curvature. As a consequence, the thickness ratio is a trade-off between a small initial deflection and a large displacement upon actuation.

3. FABRICATION

The overall fabrication process of suspended waveguide structures with integrated alignment functionality consists of two consecutive fabrication sequences, as is illustrated in figure 3. The first sequence involves the formation of a TriPleX layer stack on a silicon (Si) wafer, providing photonic waveguides. This TriPleX stack consists of three materials: a thermally grown SiO₂ bottom cladding, a silicon nitride (Si₃N₄) waveguide core, and a SiO₂ top cladding by plasma enhanced chemical vapour deposition (PECVD). Besides the waveguide core pattern, the Si₃N₄ layer also includes alignment marks, enabling the alignment of photolithography masks with the waveguide pattern. Details on the fabrication of photonic waveguides fall outside the scope of this article.

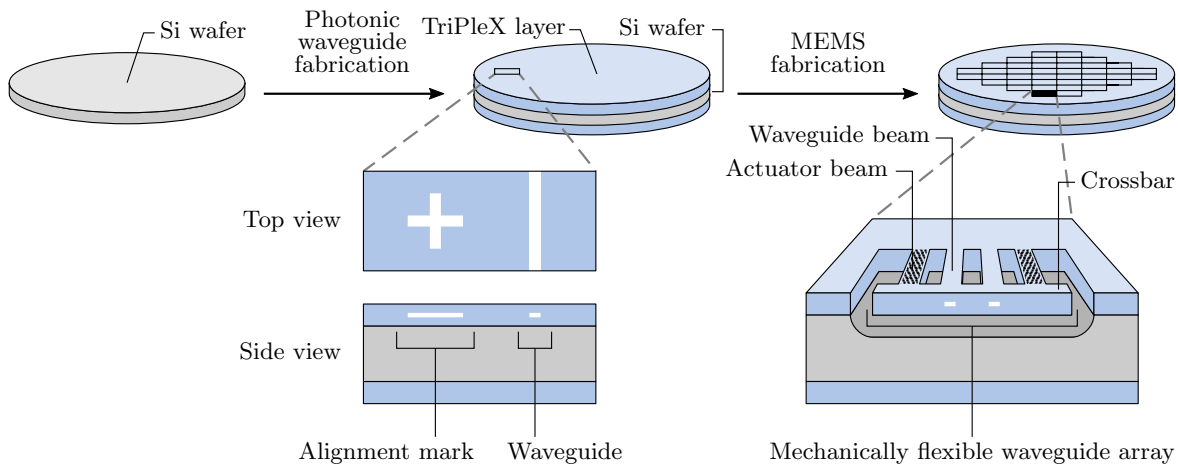


Figure 3: Schematic representation of the fabrication of positionable waveguide arrays. After fabricating the photonic waveguides, the MEMS fabrication produces suspended arrays with integrated actuators.

In the second fabrication sequence, the mechanically flexible beam arrays are created and the MEMS actuator functionality is added. This sequence can be regarded as post-processing performed after the fabrication of photonic waveguides, and is described in more detail below. The MEMS fabrication process relies on a reinforcement method that reduces the risk of beam fracturing. The residual stress within the TriPleX material causes the SiO₂ structures to fracture when they are released from a Si substrate. By temporarily reinforcing the SiO₂ beam structures with Si during the release process, fracturing of the beams is prevented. More details on the reinforcement method and its working mechanism are reported in previous work.³

The steps of fabrication sequence two are as follows. On top of a Si wafer that is provided with a TriPleX waveguiding layer, a layer of polycrystalline silicon (poly-Si()) and a layer of aluminum are deposited (figure 4a). First, a 130 nm thin seed layer of poly-Si is grown by low pressure chemical vapor deposition (LPCVD), and removed from the backside of the wafer. From this seed layer, the poly-Si thickness is increased to 3 μm by an epitaxial growth process at 1050 °C using an *ASMI Epsilon One*. Boron gas was added during the epitaxial growth, with a target sheet resistance of ~45 Ω/□ for the boron-doped poly-Si. A 0.67 μm aluminum layer, containing 1% of silicon, is sputter-deposited on top at 350 °C, using a *Trikon Sigma 204* sputter system.

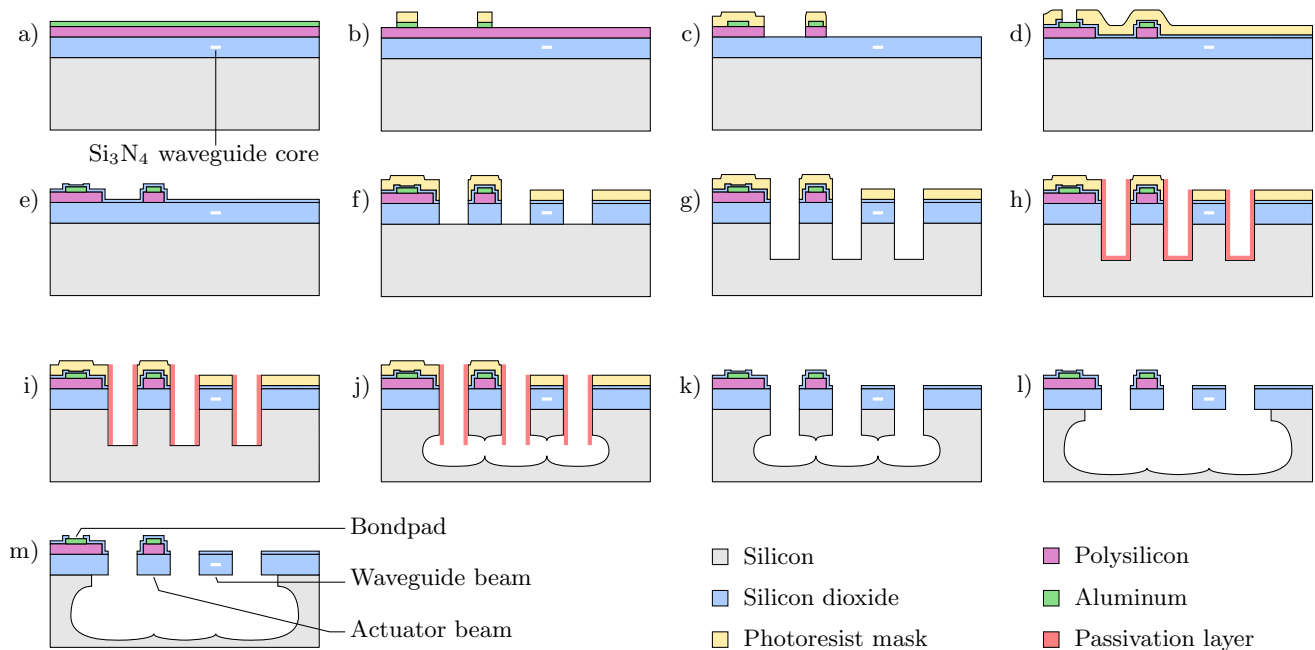


Figure 4: Fabrication steps for mechanically flexible waveguides with integrated alignment functionality. Note that only the frontside of the wafer is included in this representation. a) Deposition of poly-Si and aluminum. b) Plasma etching of the aluminum. c) Plasma etching of the poly-Si. d) Deposition of PECVD SiO₂ and local removal by plasma etching. e) Deposition of PECVD SiO₂. f) Plasma etching of SiO₂. g) Anisotropic plasma etching of Si. h) Deposition of passivation layer. i) Local removal of passivation layer. j) Isotropic plasma etching of Si. k) Removal of passivation layer. l) More isotropic etching of Si. m) Plasma etching of PECVD SiO₂, to expose the bondpads.

A 1.4 μm thick Shipley SPR3012 photoresist pattern is applied by spin coating and the aluminum is etched (figure 4b) in a *Trikon Omega 201* plasma etcher. A new 4.0 μm thick Shipley SPR3027 photoresist pattern is spin coated and used as mask during plasma etching of the poly-Si (figure 4c). The poly-Si is etched using an *SPTS Omega i2L Rapier* deep silicon etcher. After depositing a 2 μm thick PECVD SiO₂ layer that covers the complete wafer, a 4.0 μm thick Shipley SPR3027 photoresist pattern is applied and the SiO₂ is locally etched where bondpads will be realized (figure 4d). The PECVD SiO₂ is deposited in a *Novellus Concept 1* CVD system and is etched using a *Drytek Triode 384T* etcher.

Another layer of PECVD SiO₂, this time with a thickness of 0.3 μm, is deposited, covering the complete wafer

(figure 4e). AZ9260 photoresist with a thickness of $12\ \mu\text{m}$ is spin coated, patterned, and used as mask for two etching steps. First, the complete SiO_2 layer is etched in the Drytek Triode (figure 4f). After that, the same photoresist mask is used for the anisotropic plasma etching of Si (figure 4g) in the SPTS Omega i2L.

From this point on, the remaining steps are all performed using the SPTS Omega i2L Rapier deep silicon etcher. A passivation layer of approximately $1\ \mu\text{m}$ is deposited (figure 4h). This passivation layer is locally removed from the trench bottom (figure 4i). The Si that is not protected is isotropically plasma etched (figure 4j). After removal of the remaining passivation layer (figure 4k), more Si is isotropically etched (figure 4l). Finally, the bondpads are opened by plasma etching of PECVD SiO_2 (figure 4m).

A scanning electron microscope (SEM) image of a realized suspended waveguide array with integrated alignment functionality is presented in figure 5. The array consists of four waveguide beams, with four actuator beams on both sides. The beams are $800\ \mu\text{m}$ in length and $18\ \mu\text{m}$ in width, and the waveguide pitch is $50\ \mu\text{m}$.

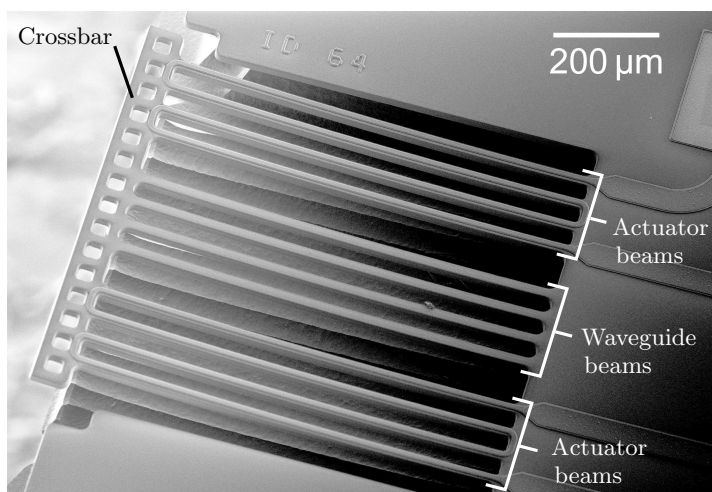


Figure 5: SEM image of realized positionable waveguide array. This image was taken with a 30° tilt.

4. CHARACTERIZATION

In this Section, the integrated alignment functionality is characterized. First, measurements of the initial deflection of the suspended structures, caused by the residual stress in the layers, are discussed. Then, the operating range of the actuators is experimentally determined. Furthermore, the positioning of the crossbar is quantified, followed by a stabilization study at a constant actuator power. Ultimately, the compatibility with the alignment concept is evaluated.

4.1 Initial deflection of the suspended structure

The surface contours of suspended structures are obtained by means of white light interferometric profilometry (Bruker Contour GT-K 3D optical profilometer). The profiles measured over the length of one waveguide beam and two actuator beams are presented in figure 6. The beams have an initial (i.e. without actuation) out-of-plane deflection. As a result, the free ends of the beams are located approximately $50\ \mu\text{m}$ above the surface of the PIC. The radius of curvature of the three measured beams ranges from $128/\text{m}$ to $136/\text{m}$, corresponding to a radius of curvature of $7.8\ \text{mm}$ and $7.3\ \text{mm}$, respectively.

In order to understand the out-of-plane deflection measurements of the suspended structure, we need to look at the components: the actuator beams, the waveguide beams and the crossbar. The actuator beams consist of SiO_2 with poly-Si on top. They have an upward curvature, caused by compressive stress in the SiO_2 and tensile stress in the poly-Si. The waveguide beams, having no poly-Si layer, do not tend to curl up that much. Measurements of comparable suspended TriPleX beams revealed an upward curvature with a radius between $200\ \text{mm}$ and $800\ \text{mm}$.⁴ The crossbar mechanically connects the free ends of the actuator beams with the free

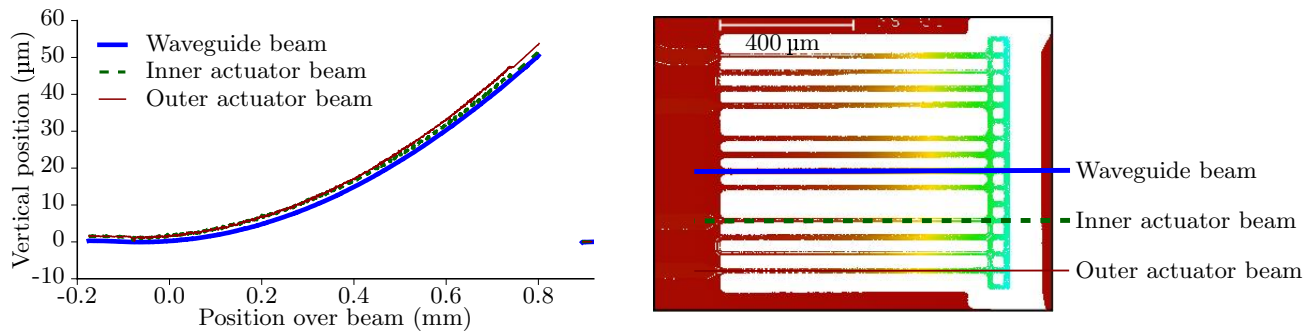


Figure 6: Left: graph showing the initial profiles (without actuation) measured over the length of three beams. Right: top view of the suspended waveguide array, indicating the locations of the three profiles.

ends of the waveguide beams. Because the actuator beams outnumber the waveguide beams (eight versus four) and they are stiffer (due to the poly-Si), they cause the waveguide beams to bend upward as well.

Figure 7 contains the profile measured over the length of the crossbar, the profile of a reference surface, and the profile measured at the base of the beams. From the profile at the base of the beams, four elevated regions can be identified, corresponding to the poly-Si pattern. Moreover, this profile indicates that the surface of the PIC is straight and horizontal. However, the profile over the length of the crossbar shows a curvature: the end points of the crossbar are located above the crossbar's center. The profile of the crossbar corresponds to a curvature of approximately $63/m$ ($= 16\text{ mm radius}$), and results from the waveguide and actuator beams connected to it. The actuator beams (situated on the outer sides of the crossbar) have a larger curvature than the waveguide beams (located in the center). Also, the outer actuator beams have a larger curvature than the inner actuator beams.

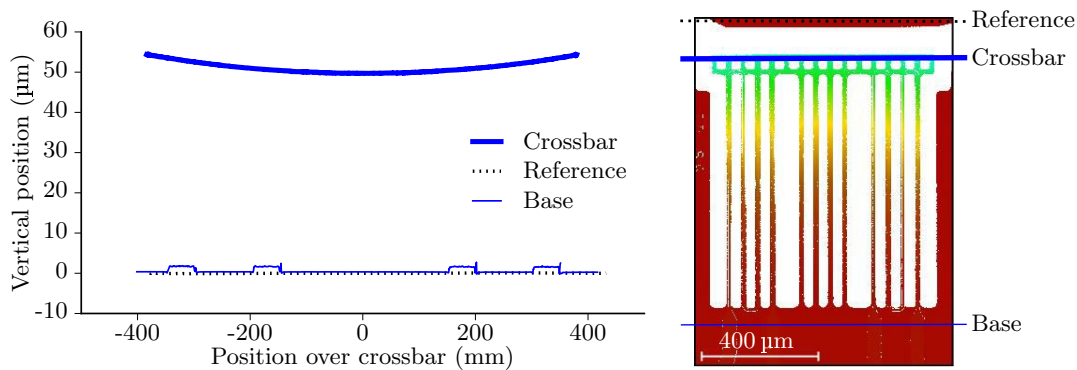


Figure 7: Left: graph showing the initial profile (without actuation) measured over the length of the crossbar. Right: top view of the suspended waveguide array, indicating the locations of the three profiles.

4.2 Actuator operating range

The actuator's operating range was determined by subjecting an actuator to increasing voltages while monitoring the resistance of the actuator. To this end, successive linear voltage ramps with increasing values for the maximum voltage were applied to the actuator, using a *Keithley 2611 SourceMeter*. The results of this experiment are plotted in figure 8. All cycles show a similar trend, i.e. the resistance first decreases and then increases with increasing voltage. Up to the third voltage ramp (with a maximum voltage of 70 V), the resistance values are very similar. Cycle 4 shows resistance values that are higher. The resistance values measured in cycle 5 are even higher. This suggests that the actuator material properties change when a voltage around 70 V or higher is applied. Moreover, the third voltage ramp shows a dramatic drop in resistance when 70 V is applied to the actuator. This is a known effect in doped poly-Si and results from an increase in intrinsic carrier concentration

with increasing temperature.^{5,6} During the experiment, at times the resistance of the actuator dramatically dropped, the current was limited by the sourcemeter's user-defined current limit. In order to obtain reproducible results, the voltage should stay below this value of 70 V. Based on figure 8, we assume that a safe operating range of this actuator is from 0 V to 45 V.

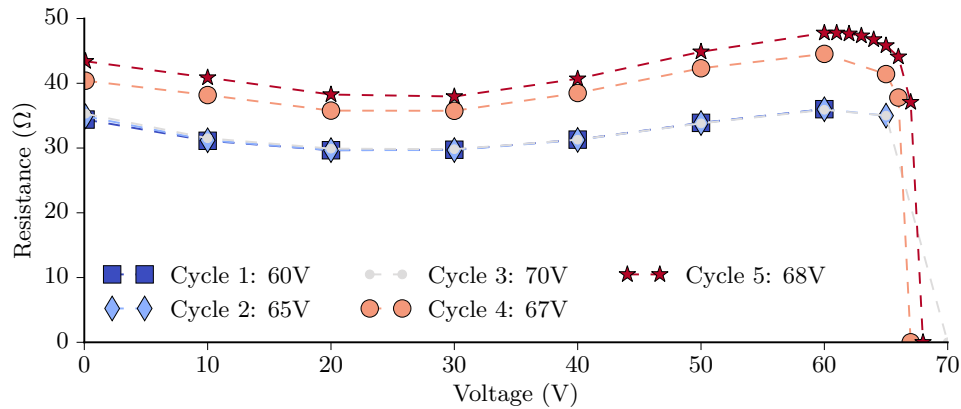


Figure 8: Graph showing the resistance as a function of voltage for successive linear voltage ramps.

4.3 Crossbar positioning by actuation

In order to make a quantitative analysis of the positioning properties of the actuators, we introduce three positioning parameters: Δy_{center} , α , and $range_{wg}$. These three parameters describe the effect of actuation on the waveguide beam end-facets and can be obtained from white light interferometric profilometry measurements. Figure 9 shows a schematic representation of the crossbar, indicating the positioning parameters.

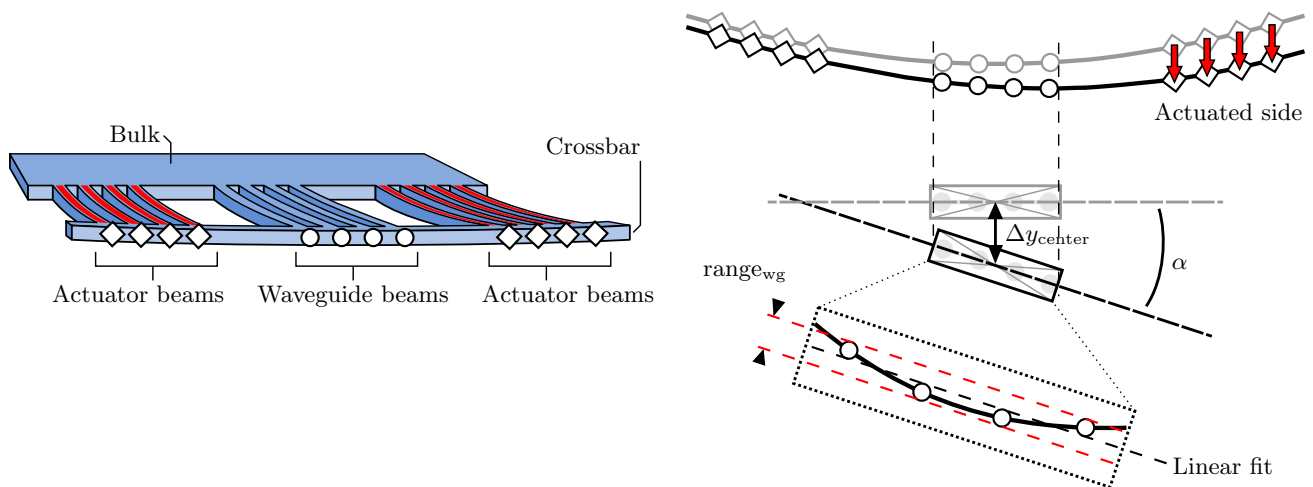


Figure 9: Schematic representation of a positionable waveguide array showing the three positioning parameters: Δy_{center} , α , and $range_{wg}$.

All three parameters use the linear approximation of the part of the crossbar where the waveguide beams are located. Δy_{center} is the change in vertical deflection of the center of the linear approximation with respect to the non-actuated situation. The angle α represents the angle between the linear approximation and a horizontal line. Finally, $range_{wg}$ quantifies the deviation of the individual waveguide end-facets from a straight line. It is defined as the max-min range of the vertical position of the waveguide beams' free ends, after subtracting the linear fit in order to level the data.

Three actuation modes were measured. (1) Operating the actuator on the left side of the waveguide array. (2) Operating the actuator on the right side of the waveguide array. (3) Operating the actuators on both sides of the waveguide array. The results of these actuation modes will be henceforth referred to as ‘left’, ‘right’, and ‘both’, respectively. Figure 10 presents one graph per positioning parameter, in which the measurements of all three actuation modes are plotted.

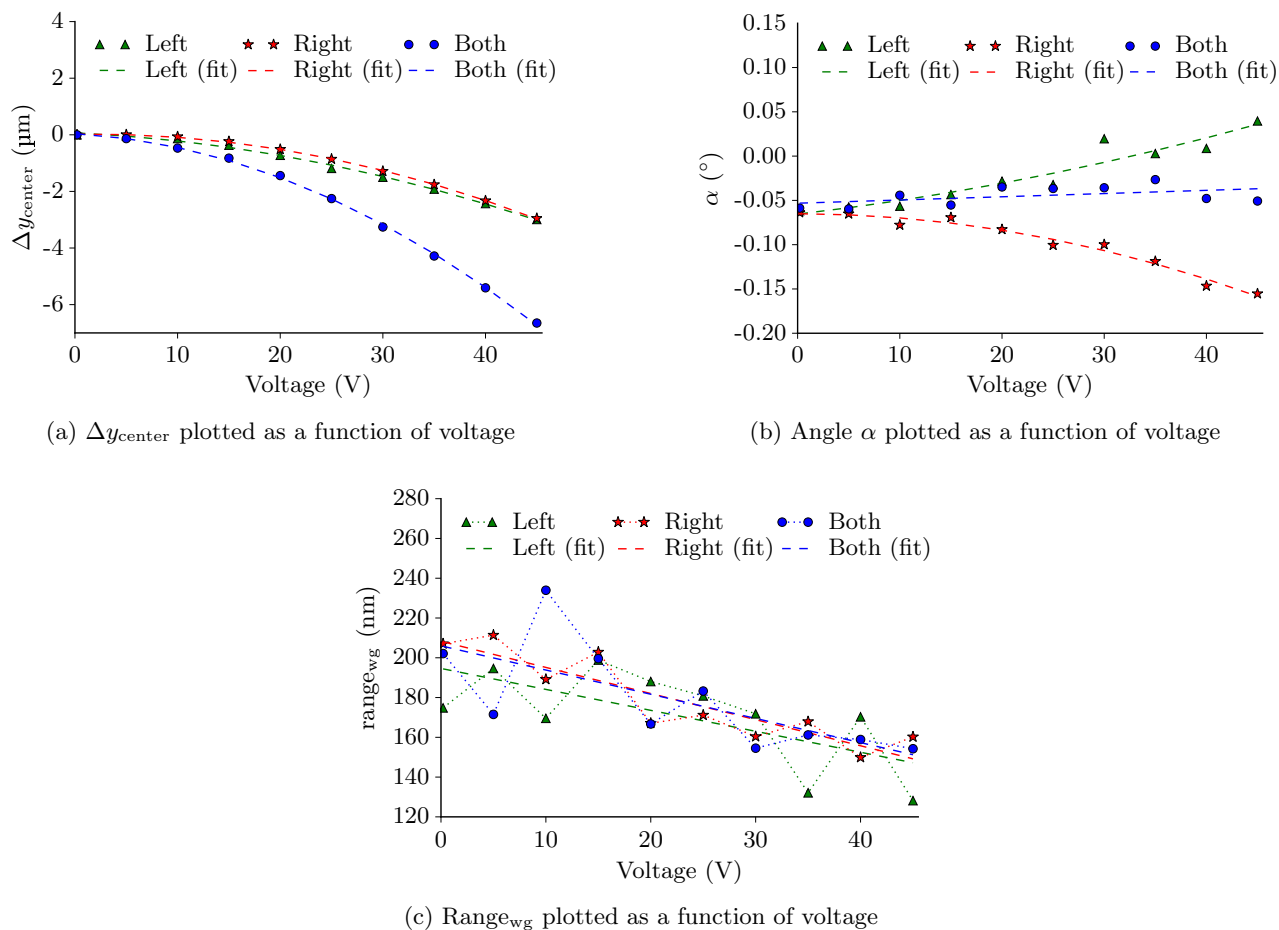


Figure 10: Plots of the three positioning parameters during actuation of the positionable waveguide structure.

The vertical displacement of the center of the linear approximation is shown in figure 10a. Operating the actuators resulted in a downward displacement. The displacement caused by operating the left actuator at a certain voltage is slightly larger than the displacement caused by the right actuator at the same voltage. This is unexpected, since the actuators are designed to be similar. However, the resistance of both circuits was measured to be dissimilar. The left actuator had a resistance of 41.5 k Ω (at 45 V), while the resistance of the right actuator was measured to be 43.9 k Ω (at 45 V). At a certain voltage, the current through the lower resistance (left) will be higher, resulting in a larger deflection. The operation of both actuators at the same time resulted in a displacement that is larger for every voltage: at 45 V, a downward displacement of ~6.5 μm was measured.

In figure 10b, the angle α is plotted as a function of actuator voltage. Without actuation, angle α was measured to be -0.06° , while 0° was expected. This is possibly caused because α was determined using a reference surface. The profile of a reference surface was subtracted from the crossbar profile in order to obtain the actual crossbar movement. If this reference surface has a tilt with respect to the crossbar, the angle α gets an offset. Operating the left actuator produces an increase in angle (up to 0.05°), while the angle decreases when the right actuator is activated (up to -0.15°). When both actuators are operated simultaneously, α remains

inside a small band around the value in the non-actuated situation. Figure 10b shows a gradual increase of α as the voltage applied to both actuators is increased. This effect can be explained by the asymmetry in actuator resistance. During operation, the two actuators were connected in parallel to a single voltage source. As a consequence, the applied 45 V generated slightly more current and power on the left side than on the right side.

Figure 10c shows that for all actuation modes, the range_{wg} decreases upon actuation. This is as expected. Without actuation, the crossbar has an initial curvature: the crossbar ends are located higher than the crossbar center. By activating the actuators, the free ends of the bimorph beams are moved downwards. As a result, actuation of one or both sides will decrease the curvature of the crossbar, decreasing the range_{wg} .

4.4 Stability over time

While continuously operating the actuators, the vertical position of the crossbar was observed over time. Measurements were performed every five minutes, for a total duration of 30 min. During this test, the two actuators were operated at a constant voltage of 45 V, corresponding to 48.8 mW in the left and 46.1 mW in the right set of bimorph beams. The results of this test are presented in figure 11.

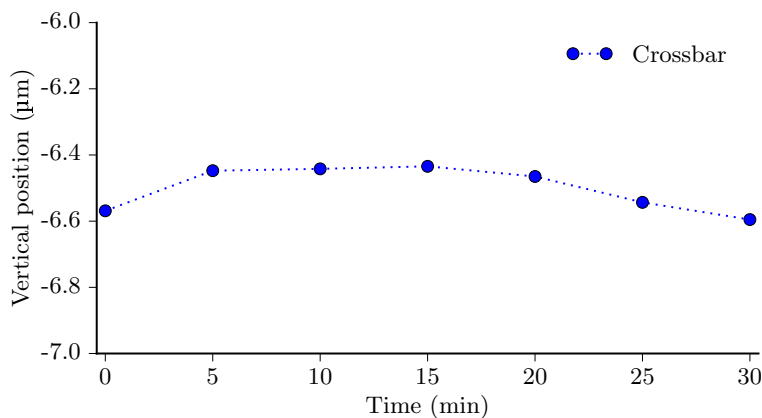


Figure 11: The vertical position of an actuated crossbar plotted over time.

The difference between the maximum and minimum crossbar position measured over 30 min amounts to $0.16 \mu\text{m}$. This is equal to a relative drift of 2.5% ($0.16 \mu\text{m} / 6.5 \mu\text{m}$). The drift does not seem to have a specific direction, and no logical explanation was found for this deviation.

4.5 Compatibility with the alignment concept

The consequence of using two out-of-plane actuators for both translating and rotating the crossbar, is that a rotation is always accompanied by a translation. In some situations, this can lead to a poor alignment. For example, suppose that after the pre-alignment, a rotational fine-alignment of 0.1° is required, while a vertical displacement of only $0.5 \mu\text{m}$ is needed. The 0.1° rotation comes with a vertical translation of more than $2 \mu\text{m}$, and it is impossible to obtain the required rotation and translation simultaneously.

Another challenge is the final out-of-plane deflection that is required for the alignment concept. For the alignment with an InP PIC, a final out-of-plane deflection of typically $\sim 6 \mu\text{m}$ is required. However, the positionable waveguide array in this paper can never meet this requirement, due to its $50 \mu\text{m}$ initial deflection and the $6.5 \mu\text{m}$ motion range.

By modifying the design, the configuration with two out-of-plane actuators can provide the rotation and translation required in the fine-alignment step. For example, changing the poly-Si thickness or using a different pitch between the beams will affect the way crossbar translation and rotation interact. In a related European research project, the actuation with poly-Si patterned on a part of the SiO_2 beams is investigated.⁷

The realized integrated alignment functionality provides rotation and out-of-plane translation of the crossbar. In-plane translation was not implemented in the characterized system. However, the alignment concept does rely on in-plane fine-alignment. In future designs, actuators for in-plane alignment will be included.

5. CONCLUSIONS AND PROSPECT

This paper has demonstrated the fabrication and characterization of a positionable photonic waveguide array. By using a special reinforcement method, the compressive-stress-induced fracturing of SiO₂ beams was prevented. Thermal out-of-plane bimorph actuators were realized by fabricating beams consisting of poly-Si on top of SiO₂.

Interferometric profilometry measurements showed that, without actuation, the entire suspended beam structure curves upward. Over the length of the beams, a radius of curvature of approximately 7.5 mm causes the free end to rise 50 μm above the chip surface. This initial deflection at room temperature results from thermal stress in the bimorph actuator beams. Out-of-plane actuators at the left and right side of the crossbar enable downward out-of-plane translation (up to 6.5 μm) and rotation around the propagation direction of the waveguides ($\pm 0.1^\circ$), with a relative drift of 2.5%. The rotational and translational actuation ranges are sufficient for the alignment concept. However, more research into different designs is required to enable full compatibility with the alignment concept.

Future research will include the characterization of suspended structures with different parameters, like the beam length, the beam pitch, and the poly-Si pattern. Moreover, the implementation of in-plane actuators will be studied. Additionally, a system for locking the position of the crossbar will be developed.

ACKNOWLEDGMENTS

The research leading to the presented results has received funding from the STW Generic Technologies for Integrated Photonics (GTIP) programme, grant no. 11355 (Flex-O-Guides). We are grateful to Tom Scholtes and Johan van der Cingel at the Else Kooi Laboratory for the support in microfabrication.

REFERENCES

- [1] Wörhoff, K., Heideman, R. G., Leinse, A., and Hoekman, M., “TriPleX: a versatile dielectric photonic platform,” *Advanced Optical Technologies* **4**(2), 189–207 (2015).
- [2] Chu, W.-H., Mehregany, M., and Mullen, R. L., “Analysis of tip deflection and force of a bimetallic cantilever microactuator,” *Journal of Micromechanics and Microengineering* **3**(1), 4–7 (1993).
- [3] Peters, T.-J. and Tichem, M., “Fabrication and characterization of suspended beam structures for SiO₂ photonic MEMS,” *Journal of Micromechanics and Microengineering* **25**(10), 105003 (2015).
- [4] Peters, T.-J. and Tichem, M., “Mechanically flexible waveguide arrays for optical chip-to-chip coupling,” *Proc. SPIE* **9760**, 97600D–97600D–11 (2016).
- [5] Chui, B. W., Asheghi, M., Ju, Y. S., Goodson, K. E., Kenny, T. W., and Mamin, H. J., “Intrinsic-carrier thermal runaway in silicon microcantilevers,” *Microscale Thermophysical Engineering* **3**(3), 217–228 (1999).
- [6] Lee, J., Beechem, T., Wright, T. L., Nelson, B. A., Graham, S., and King, W. P., “Electrical, thermal, and mechanical characterization of silicon microcantilever heaters,” *Journal of Microelectromechanical Systems* **15**, 1644–1655 (Dec 2006).
- [7] Wu, K., Peters, T.-J., Tichem, M., Postma, F., Prak, A., Wörhoff, K., and Leinse, A., “Bimorph actuators in thick SiO₂ for photonic alignment,” *Proc. SPIE* **9753**, 975311–975311–9 (2016).